




Please cite the Published Version

Rakhimbekov, Kakhramon, Potgieter, Johannes , Valiev, Damir, An, Vladimir, Blinova, Anna , Usoltseva, Natalia , Pustovalov, Alexey, Vasilevichev, Maksim, Platonova, Alexandra, Stepanov, Sergey, Kokotov, Dmitri and Sypchenko, Vladimir (2024) WS₂-ZnO Nanostructures for Photoelectrochemical Hydrogen Generation. ACS Applied Energy Materials. ISSN 2574-0962

DOI: <https://doi.org/10.1021/acsaem.4c01488>

Publisher: American Chemical Society (ACS)

Version: Published Version

Downloaded from: <https://e-space.mmu.ac.uk/637013/>

Usage rights:  [Creative Commons: Attribution 4.0](https://creativecommons.org/licenses/by/4.0/)

Additional Information: This is an open access article which first appeared in ACS Applied Energy Materials

Enquiries:

If you have questions about this document, contact openresearch@mmu.ac.uk. Please include the URL of the record in e-space. If you believe that your, or a third party's rights have been compromised through this document please see our Take Down policy (available from <https://www.mmu.ac.uk/library/using-the-library/policies-and-guidelines>)

WS₂–ZnO Nanostructures for Photoelectrochemical Hydrogen Generation

Kakhramon Rakhimbekov, Johannes Potgieter,* Damir Valiev, Vladimir An, Anna Blinova, Natalia Usoltseva, Alexey Pustovalov, Maksim Vasilevichev, Alexandra Platonova, Sergey Stepanov, Dmitri Kokotov, and Vladimir Sypchenko

Cite This: <https://doi.org/10.1021/acsaem.4c01488>

Read Online

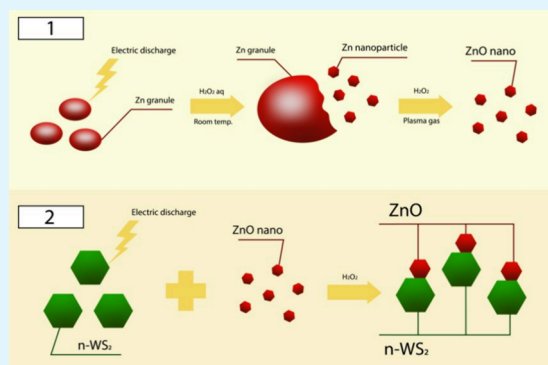
ACCESS |

Metrics & More

Article Recommendations

ABSTRACT: WS₂–ZnO nanostructured materials are of great interest in the area of green energy due to their potential application for hydrogen generation. In the present work, we report an efficient method to produce WS₂–ZnO nanoheterostructures through electrospark erosion of zinc granules in aqueous solutions of hydrogen peroxide, with the simultaneous addition of nanostructured WS₂. WS₂–ZnO nanostructures prepared with this synthesis method were carefully characterized by XRD, TEM, BET, FTIR, UV–vis, and Raman spectroscopy analyses to establish their chemical compositions and morphology. According to the XRD analysis, the resulting electrospark erosion products represent heterostructures containing individual phases of hexagonal tungsten disulfide and zinc oxide. The crystallite sizes varied from 4.3 to 66.7 nm for both phases. This correlated with the TEM measurements. Cyclic voltammetry (CV) and electrochemical impedance spectroscopy (EIS) showed that the WS₂–ZnO nanostructure decorated electrodes displayed improved conductivity, photocurrent density (by 2.564 mA/cm²), and hydrogen gas evolution under light conditions in contrast to the dark experiments. The investigation confirmed the potential of the WS₂–ZnO nanostructures for efficient hydrogen generation for green energy applications.

KEYWORDS: nanostructures, tungsten disulfide, zinc oxide, photocatalytic materials, electrospark erosion



1. INTRODUCTION

There is a worldwide drive to significantly reduce the use of fossil fuels due to their impact on climate change and their contribution to ever-increasing greenhouse gas emissions. The importance of an alternative fuel source such as hydrogen is evident. The generation of green hydrogen, such as splitting of the water molecule, has received a lot of attention recently.

Photoelectrochemical (PEC) cells use sunlight to carry out solar-to-fuel conversion, thereby splitting the water molecule using electrolysis to produce green hydrogen. Although an attractive method to use, it requires the use of expensive scarce metals, such as platinum group metals (PGMs) as electrodes. Consequently, researchers are constantly on the search for alternative materials to rival the efficiency of PGMs without the associated cost penalty. This is a critical issue to be addressed in any device utilizing sunlight conversion to produce hydrogen by water splitting for use in the production of clean energy.¹

Over the past two decades, ZnO is one of the most studied and widely applied materials for photocatalytic devices and applications due to it being widely available at low production cost and is nontoxic. It is a semiconductor material with a

bandgap of 3.37 eV, which absorbs light in the blue and ultraviolet regions of the visible spectrum. ZnO can easily be modified and transformed into nanostructures,^{2,3} which is beneficial for its use in PECs. Over the past decade, many reports have been published on the synthesis of ZnO nanoparticles,⁴ nanoflakes,⁵ hexagonal prismatic rods,⁶ nanoflowers,⁷ nanorods,⁸ nanopillars, or nanosheets, using several different synthesis methods.⁹ These studies have shown that the morphology and physical properties of the ZnO play a very important role in determining and modifying its optoelectronic properties and continue to receive increasing attention from researchers worldwide.

One example of this is doping ZnO with rare earth elements as well as cationic or anionic substitutions.^{10,11} In addition, the

Received: June 15, 2024

Revised: October 22, 2024

Accepted: October 24, 2024

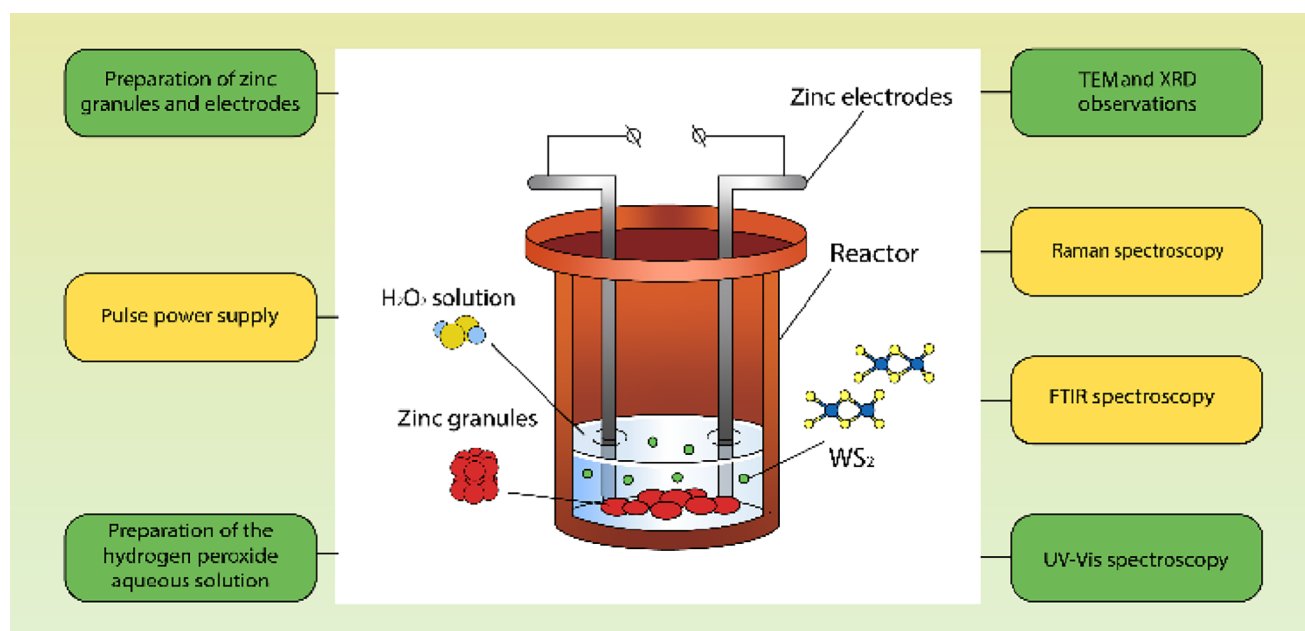


Figure 1. Scheme illustrating the fabrication and subsequent characterization techniques of the WS₂-ZnO nanostructures.

optical properties of bulk ZnO can be modified by nanostructuring. This will increase the number of intrinsic defects in the crystal structure. Alternatively, a reduction in crystal size leads to a significant increase in the surface-to-volume ratio, thereby creating stronger surface defects related to the emission. For example, rose-like ZnO exhibits enhanced fluorescent properties.¹² Diamond-shaped ZnO nanostructures deposited on dye-sensitized solar cells showed an increase in the short-circuit current.¹³ A recent study also showed that ZnO nanoparticles can exhibit interesting optical properties if the appropriate precursor was selected.¹⁴ It confirms that photoluminescent emission of ZnO can be modified by creating O and Zn vacancies. However, a remaining disadvantage is the wide bandgap of ZnO, which limits its use to being an ultraviolet photocatalyst and results in only 5% of sunlight captured by ZnO. Thus, shifting the optical response to the visible range would improve its photocatalytic efficiency. This can be achieved by doping it with metals and nonmetals and through the synthesis of heterostructures.^{15,16}

However, ZnO nanoparticles alone may not allow for enough electron transport. This can be ascribed to two reasons: first, there is insufficient contact between the particles; and second, even if there is contact between particles, grain boundaries are formed, which will interfere with electron transport. The result is that the possible fabrication of devices will be impaired. Despite its limitations, e.g., rapid recombination of photogenerated electron-hole pairs, ZnO is widely explored for large-scale use such as water and air purification.^{9,17}

A new class of photocatalytic materials attracting increasing interest because of their excellent catalytic and optical characteristics is transition-metal dichalcogenides. For example, they have been applied for photoelectrochemical water splitting to produce hydrogen for clean energy devices.^{18–20} Chu et al.²¹ showed that a p-type composite material of WS₂ has a photocatalytic activity as the photocathode of a photoelectrochemical cell under simulated solar light irradiation. Lin et al.²² found that the electronic structure and optical properties of the hybrid nanomaterials depend on the

structure of the ZnO substrates. If MoS₂ and WS₂ monolayers are present on a ZnO substrate, then the photoabsorption in the visible region of the solar spectrum is enhanced. Because the increase of ZnO substrate thickness decreases absorption ability, investigations should focus on the synthesis of thin film ZnO. Wang et al.²³ investigated the structural, electronic, and optical properties of heterostructures and found that type-II band alignment occurred at the WS₂/ZnO interfaces. Thus, there is a split of the photogenerated electron-hole pairs at the surface (conduction-band minimum (CBM) and valence-band maximum (VBM) located in the different layers), which determines the various photovoltaic and photocatalytic efficiencies of the heterostructures. A water decomposition process depends on the correlation of the CBM/reduction potential of water and the VBM/oxidation potential of water. Guan et al.²⁴ observed that adjustment of CBM and VBM provides a suitable material for the successful application of water splitting.

There is limited work on the new class of transition-metal dichalcogenide photocatalytic materials available in the literature. WS₂ combinations, in particular, have only been described in a handful of papers. The effect of its synthesis, morphology, and crystal size on its performance can clearly be extended and benefit from more investigations and new knowledge. The present work describes a hitherto unexplored fabrication method of nanoheterostructures by electrospark erosion (ESE) and their characterization as potential photoelectrode materials for hydrogen generation in photoelectrochemical cells. The electrospark erosion technique was used to produce binary composite materials in the WS₂-ZnO system and evaluate their efficiency for hydrogen generation when water is split. Not only will this add new knowledge to the field about WS₂-ZnO heterostructures but also will contribute to unlocking a viable cheap and efficient method for large-scale hydrogen generation for energy applications.

2. MATERIALS AND METHODS

2.1. Preparation of WS₂-ZnO Nanostructures. The WS₂-ZnO (WZO) nanoheterostructures were manufactured by electro-

spark erosion (ESE).²⁵ This technique is a hybrid of top-down and bottom-up approaches: with a decrease in the particle diameters (WS₂ and Zn), an increase in the size of the heterostructure components occurs. The method of electrical explosion of the conductor (tungsten wire) was used to produce tungsten powder. The passing of high-density pulsed current through a conductor results in the intense energy release, the generation of shock waves, and creating the possibility of rapid heating of the metal to temperatures above 10⁴ K. This leads to a change in the physical state of the metal and the formation of nanodispersed particles of the metal (tungsten) from which the conductor is made. Nanodispersed tungsten powder was mixed with elemental sulfur and pressed into tablets, and nanostructured tungsten disulfide WS₂ was obtained by self-propagating high-temperature synthesis (SHS). The combustion process was initiated by local heating of the sample (tablet) using a nichrome spiral through which a current pulse was passed. After initiation at a single point, the combustion front spread over the surface of the sample from the center to the periphery. Then, a bright glow was observed from the surface of the sample, which gradually covered the entire sample. The exothermic effect of the interaction of nanodispersed tungsten powder and elemental sulfur provides the synthesis of tungsten sulfide by the SHS method in an autowave mode with the maintenance of a combustion wave due to the thermal effect of a chemical reaction. WS₂-ZnO nanostructures were synthesized by ESE of zinc granules (analytic grade, ZAO "Soyuzhimprom", Novosibirsk, Russia) in aqueous solutions of hydrogen peroxide (OOO "INNOVATSIIA", Voronezh, Russia), with the simultaneous addition of WS₂ nanostructured powder in the reaction zone. Nanostructured tungsten disulfide was prepared by the self-propagating high-temperature synthesis of mixtures of tungsten nanopowder and elementary sulfur. The scheme of the ESE experiment for the preparation of the WS₂-ZnO heterostructures is presented in Figure 1. The schematic diagram shows a reactor, which is a porcelain vessel that can withstand strong impulses of an electric current. During the pretreatment stage, zinc granules are dispersed in hydrochloric acid and dried afterward in order to remove the oxide film from the surface of the granules. A high-energy pulse power supply was used to provide current according to the experimental protocol. Aqueous solutions of hydrogen peroxide at various volume concentrations were used in the different runs to prepare the WS₂-ZnO heterostructures. The experimental protocol requires the preparation of 5 volume concentrations of a 38% solution of hydrogen peroxide to determine the effect of its concentration in the formation of the WZO nanostructures.

A 38% solution of hydrogen peroxide (SHP) was used as a liquid-solvent oxidizer in the electrospark experiments. The basic SHP was dissolved in distilled water in 4 different volume concentrations: 100, 75, 50, and 25, while distilled water was used as a fifth solution (0%). The aim was to evaluate the role of hydrogen peroxide concentrations in the formation processes of ZnO nanoparticles and WS₂-ZnO heterostructures. A mass of 185 g of zinc granules was weighed for each series of experiments and was then placed into the reactor before 200 mL of SHP was poured in as well. After this procedure, electric current pulses were applied to the electrodes from the power supply, lasting 30 s for each experiment. The following experimental conditions were applied during testing: electrode separation distance of 10 cm, voltage of 500 V, current of 150 A. After each experiment, the prepared suspension was separated into two fractions (the small-size (S) and large-size (L) fractions). Both fractions were initially suspensions of the as-prepared nanostructured particles before they were subsequently separated using the principle of different sedimentation rates. The obtained fractions were dried at 80 °C in an oven for 1 h. The synthesized WS₂-ZnO heterostructures were characterized by various analytical methods, such as transmission electron microscopy (TEM), X-ray diffractometry (XRD), Raman and Fourier transformation infrared (FTIR) spectroscopy, ultraviolet-visible spectroscopy (UV-vis), cyclic voltammetry, and electrochemical impedance spectroscopy.

2.2. Characterization Techniques. X-ray diffraction (XRD) diffractometry was carried out using a Shimadzu-7000S diffractometer

(Cu K α radiation, $\lambda = 1.5418$ Å, Shimadzu, Kyoto, Japan) in order to examine the crystal structures of the heterostructures prepared by electrospark erosion. Transmission electron microscopy (TEM) and energy-dispersive X-ray spectroscopy (EDS) analysis were performed on a JEOL JEM-2100F instrument (JEOL Ltd., Tokyo, Japan) for morphological observations and chemical compositions of the prepared nanoheterostructures. The specific surface area of the prepared samples was determined on a specific surface area analyzer SORBTOMETER-M (Granat, Russia) employing the BET and STSA multipoint methods. The specific surface areas of the prepared WS₂-ZnO nanostructures were measured in triplicate at $p/p_0 = 0.2$. Fourier transform infrared spectroscopy of the synthesized samples was conducted on an FTIR spectrometer (Shimadzu, IRAffinity-1S) in the range of wavenumbers from 500 to 4000 cm⁻¹. The resonance modes and valence states of the prepared heterostructures were analyzed using Raman spectroscopy (Centaur-HR, Russia) with a 532.8 nm excitation laser. The reflectance spectra of the studied samples were captured using an AVASPHERE-50-LS-HAL integrating sphere and Avantes AvaSpec-3648 fiber spectrometer in the 200–1000 nm spectral range. A Xenon 150W light source with an operating range of 200–2500 nm was used as a source of probing radiation. A MS-20 glass reference was applied to reduce the effect of reflection from the sample surface.

3. RESULTS AND DISCUSSION

3.1. Particle Size, Morphology, and Phase Compositions of the Synthesized WS₂-ZnO Nanostructures. WS₂-ZnO nanostructures were prepared via a facile electrospark erosion process where zinc granules were dispersed in aqueous solutions of hydrogen peroxide with the simultaneous addition of WS₂ nanostructured powder into the reactor. The marking list and main characteristics of the WZO heterostructures are given in Table 1. The used abbreviations are

Table 1. List of the Samples of WZO Nanostructures Prepared by the ESE Method in H₂O₂ Aqueous Solutions

sample	38% H ₂ O ₂ (v/v)	surface area, (m ² /g)
WZO-1S	100	9.4
WZO-1L	100	15.1
WZO-2S	75	24.8
WZO-2L	75	27.6
WZO-3S	50	34.0
WZO-3L	50	35.0
WZO-4S	25	23.5
WZO-4L	25	23.9
WZO-5S	0	101.1
WZO-5L	0	4.4

linked to the dimensions of structural elements in two main WZO fractions decanted from the working ESE suspensions after drying: small-size (S) and large-size (L) fractions. Table 1 demonstrates that the small-size fractions have a smaller specific surface area compared with the large-size fractions, except for the case where no hydrogen peroxide was present in the solution.

Transmission electron microscopy observations demonstrated the presence of nanostructured WS₂-ZnO in the final products (Figure 2). The zinc oxide particles are 20–40 nm in diameter, whereas the larger hexagonal tungsten disulfide particles have average sizes of 40–80 nm. The ZnO and WS₂ nanoparticles adhere to each other due to the formation of active centers formed during electrospark dispersion. Initial tungsten disulfide particles were hexagonal "sandwiches"

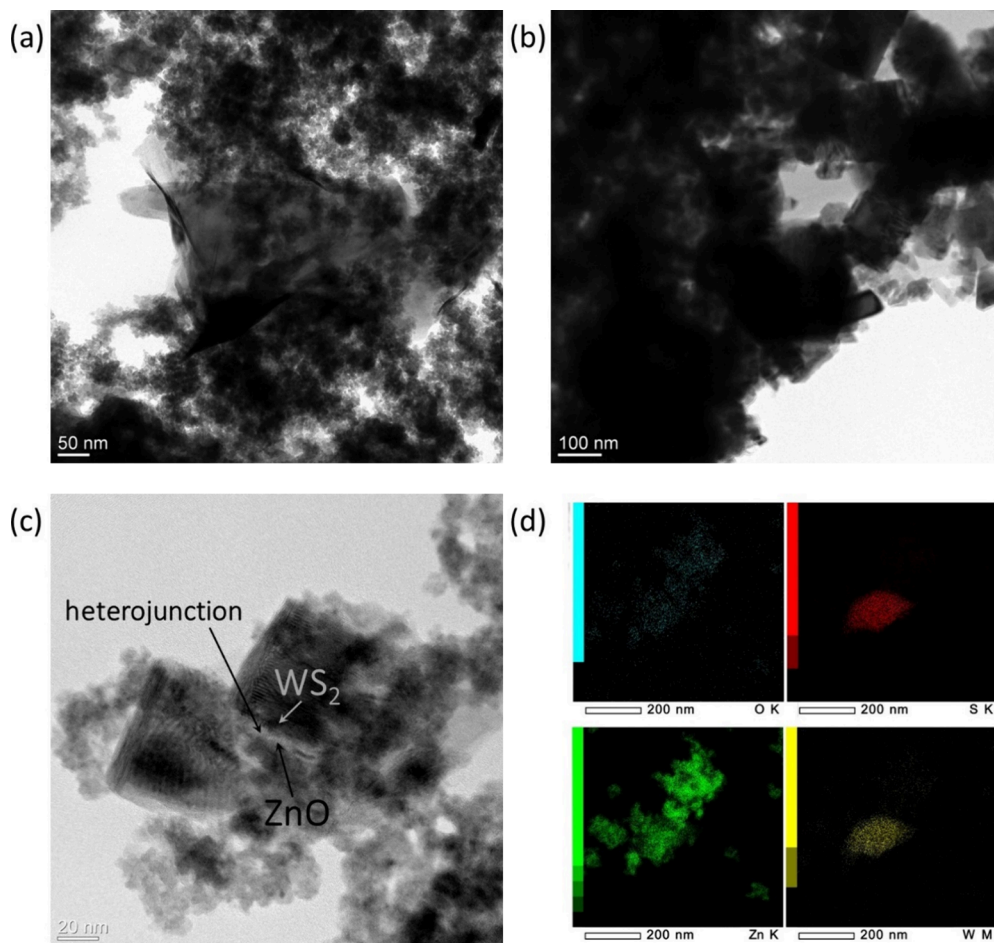


Figure 2. TEM image of the prepared WZO nanostructures.

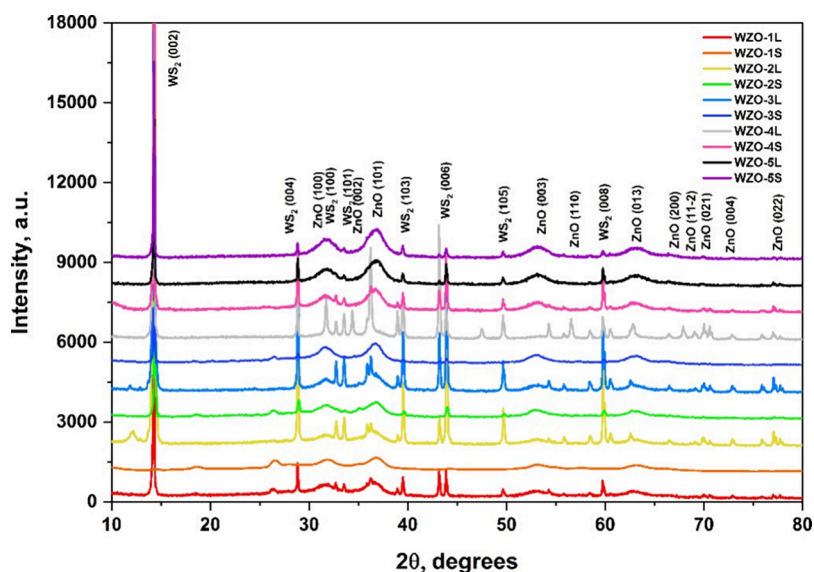


Figure 3. XRD patterns of the WZO nanostructures prepared by the ESE method.

formed due to van der Waals packages, which were delaminated during the ESE process.

The X-ray diffraction (XRD) patterns of the WS_2 -ZnO (WZO) nanostructures are presented in Figure 3. Only two crystalline phases were detected: hexagonal ZnO (zincite, PDF card No. 036-1451) and hexagonal WS_2 (PDF card No. 08-

0237). According to the XRD patterns of the WS_2 -ZnO heterostructures, ZnO reveals (100), (002), (101), (102), (003), (110), (013), (200), (11-2), (021), (004), and (022) diffraction planes, whereas the WS_2 displays (002), (004), (100), (101), (103), (006), (105), and (008) diffraction maxima. According to the XRD observations in Figure 3, the

tungsten disulfide used did not reveal any chemical or polymorph transformation during electrospark erosion.

The crystallite size D of the WS_2 -ZnO nanostructures was calculated from the XRD data according to the Sherrer equation:

$$D = \frac{K\lambda}{\beta \cos\theta}$$

where K is a unitless constant taken as 0.9, λ is the X-ray wavelength (1.54 Å), β is the width of the line at half-maximum intensity, and θ is half of the diffraction angle. The D values were determined for the three highest and most intense peaks of the WS_2 and ZnO spectra.

The determination of the chemical bonds and functional groups was conducted by Fourier-transform infrared spectroscopy (FTIR) in the transmittance mode. The FTIR spectra were captured for all WZO nanostructures, prepared under different concentration conditions, as shown in Figure 4. The

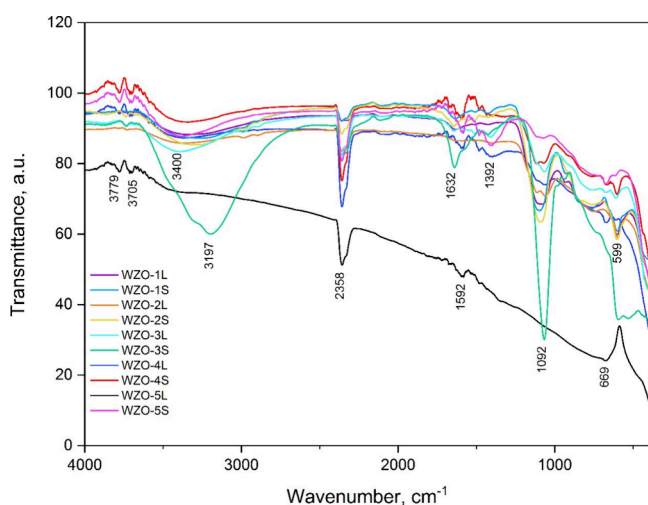


Figure 4. FTIR spectra of the nanoheterostructures WS_2 -ZnO.

distinctive bands detected and their assignments are summarized in Table 2. Specific characteristics of the ZnO lattice, related to fundamental aspects of WS_2 -ZnO, can be detected in all WZO nanoheterostructures prepared in different hydrogen peroxide concentrations. Some important features, such as stretching Zn-O modes due to the hexagonal wurtzite phase, appear as strong peaks in all the WZO heterostructures. This is an important feature indicating potential energy harvesting. The 599 and 669 cm^{-1} positions in all FTIR spectra are characterized by bonding and stretching Zn-O²⁶ modes. The peaks at 1092 cm^{-1} are due to S-S

bonds,²⁷ while the peaks at 1392 and 1632 cm^{-1} are related to hydroxyl groups.²⁷ The band at 2358 cm^{-1} can be attributed to CO_2 vibrations related to the presence of atmospheric air^{28,29} and can be linked to the possible aeration during the electrospark erosion, drying, or storing (in the case of the pure tungsten disulfide powder). The broad absorption band at 3400 cm^{-1} can be assigned to the stretching vibrations of the O-H group.³⁰

Figure 5 shows the Raman spectra of various WZO nanoheterostructures. The nature of the high-intensity

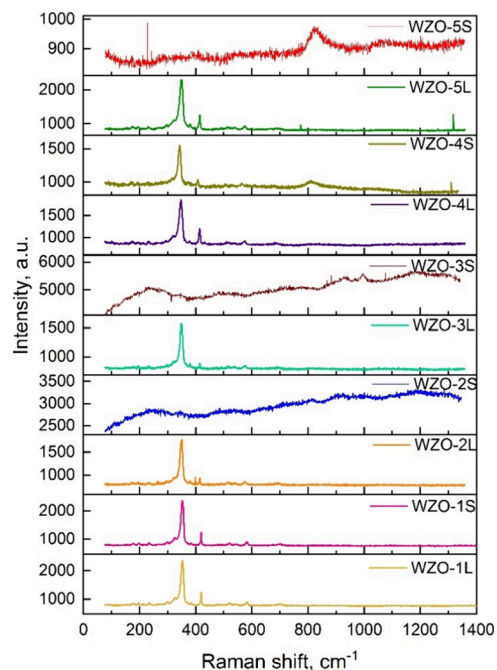


Figure 5. Raman spectra of the prepared WZO nanoheterostructures.

absorption band at 245 cm^{-1} may be due to internal zinc defects in the structure of zinc oxide for the small fraction sample WZO-1S. The peak in the Raman spectrum at 508 cm^{-1} can be assigned to the $3E_1(TO)+E_{2L}$ multiphonon mode of zinc oxide. The band at 176 cm^{-1} apparently refers to the LA longitudinal phonon mode of tungsten disulfide WS_2 .³¹ The bands at 230 and 297 cm^{-1} are assigned to the A_{1g} -LA and $2LA-E_{2g}$ modes of tungsten disulfide, respectively. The shifts at 353 and 419 cm^{-1} belong to the E_{2g}^1 and A_{1g} out-of-plane vibrational modes of WS_2 . The experimental results obtained are in good agreement with previous studies on WS_2 Raman spectroscopy.³² The other two peaks observed at 325 and 581 cm^{-1} correspond to the $3E_{2H}+E_{2L}$ multiphoton scattering mode as well as the $E_1(LO)$ fundamental phonon mode of ZnO,

Table 2. Description of the Position and Interpretation of FTIR Absorption Bands of the WS_2 -ZnO Nanostructures^a

band positions, cm^{-1}										assignment
WZO-1S	WZO-1L	WZO-2S	WZO-2L	WZO-3S	WZO-3L	WZO-4S	WZO-4L	WZO-5S	WZO-5L	
599 c	599 c	599 c	599 c	599 w	599 w	599 w	599 w	599 w	599 w	bonding Zn-O modes
699 c	699 c	699 w	699 w	699 c	699 w	699 w	699 w	699 w	699 w	stretching Zn-O modes
1092 c	1092	1092 c	1092 c	1092 c	1092 c	1092 c	1092 c	1092 w	1092 w	S-S bond modes
1632 w	1632 w	1632 w	1632 w	1632 c	1632 w	1632 w	1632 w	1632 w	1632 w	modes of hydroxyl groups
2358 c	2358 w	2358 c	2358 c	2358 c	2358 c	2358 c	2358 c	2358 c	2358 c	CO_2 vibrations (atmosphere)
3400 b	3400 b	3400 b	3400 b		3400 b	3400 b	3400 b	3400 b	3400 b	O-H group stretching

^ac = clear; w = weak, b = broad.

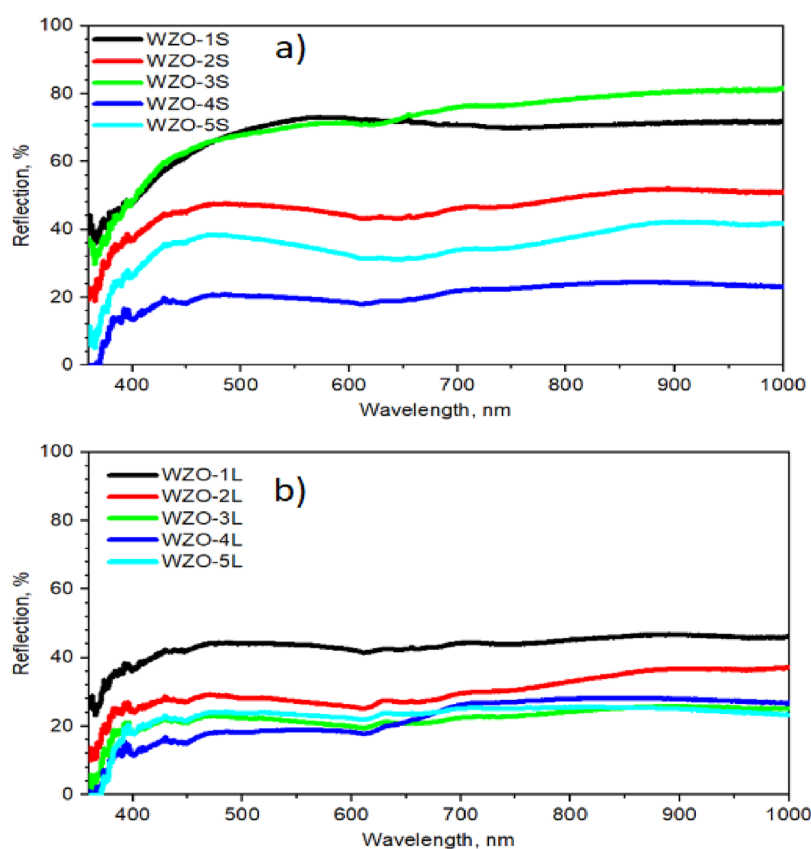


Figure 6. Reflection spectra of the prepared WZO nanostructures (a) small and (b) large particle sizes.

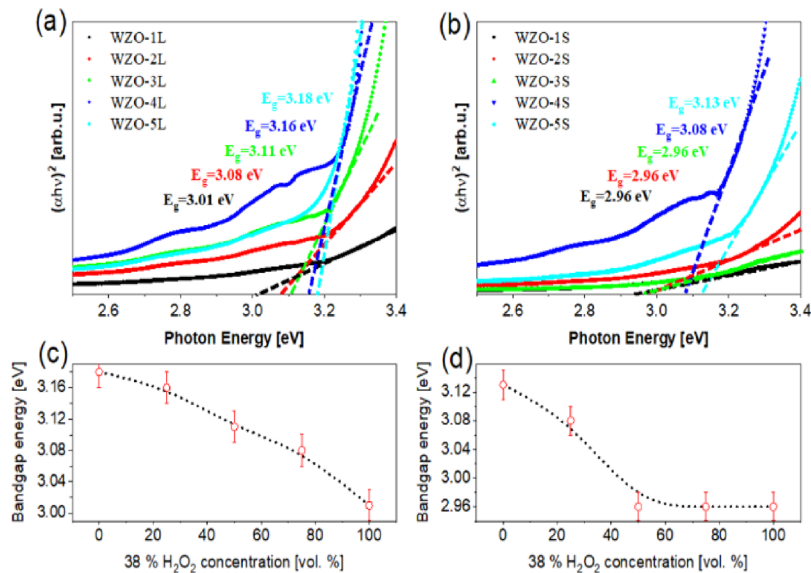


Figure 7. Tauc plots of the WZO heterostructures with various size fractions (a, b). Variation of the bandgap energy of WS_2 -ZnO nanoheterostructures according to the H_2O_2 concentration of the original 38% solution used in the ESE procedure (c, d).

respectively.³³ The shift at 953 cm^{-1} can be attributed to the flat mode of zinc oxide of sample WZO-3S, whereas the shift at 835 cm^{-1} corresponds to the ZnO mode. There are some particularly noticeable features of the samples prepared in distilled water. The shift at 835 cm^{-1} observed in the Raman spectrum of the WZO-5S sample (prepared in distilled water) for example may relate to the mode of zinc oxide in the nanostructured state.³⁴

There is a shift at 199 cm^{-1} in the Raman spectrum of the large fraction of the sample prepared in distilled water, which probably belongs to the A_1 mode of zinc oxide.

3.2. Optical Properties. Figure 6a,b shows the total (diffuse) reflection results of the various prepared oxide-sulfide nanoheterostructures in the ultraviolet, visible, and near-infrared spectral regions. The maximum reflection coefficient corresponding to the WZO-3S sample is about 78% in the IR spectral region. A similar value is assigned to the WZO-1S

sample in the visible spectral region. However, there is a decrease in the reflection coefficients in the IR region for this sample. The minimum reflection coefficients obtained are for the WZO-4S sample, and it is about 19% of the spectrum. In the reflection spectra, absorption bands can be identified at 400 and 450 nm, similar to those of the oxide–oxide nanoheterostructures discussed above. At the same time, bands are detected at 610, 650, and 750 nm. There is a shift of the fundamental absorption boundary in the oxide–oxide systems. For the WZO series samples with the large-scale structure represented in Figure 6b, the maximum reflection corresponds to the WZO-1L sample and it is about 42% of the spectrum. WZO-3L, WZO-4L, and WZO-5L samples have similar values of the reflection coefficient at approximately 20%. Absorption bands at 400 and 450 nm can be detected in the reflection spectra. There are bands at 610, 650, and 750 nm, which indicates that there is a shift of the fundamental absorption boundary.

To estimate the band gap of the samples based on the reflection spectra measurements, the Kubelka–Munk transformation was used (Figure 7a,b). The exponent depending on the type of optical transition was assumed to be equal to 1/2. The bandgap energies of WZO with the small and the large scale crystal sizes decrease from 3.13 to 2.96 eV and 3.18 to 3.01 eV, respectively (Figure 7c,d). The results obtained are consistent with the results obtained by other authors.^{35,36} The difference in bandgap values was caused by the variation in the crystal structure of WS₂, depending on the H₂O₂ concentration used in its synthesis.

3.3. Photoluminescence Properties. There is a weak emission band observed upon excitation at a wavelength of 305 nm for WZO-1S, 2S, 3S, 4S, and 5S samples in the 350–700 nm spectral region (Figure 8a) Three emission bands can be

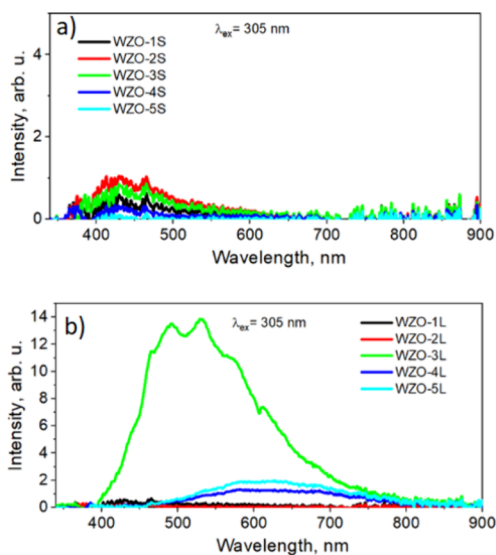


Figure 8. Photoluminescence spectra of the various WZO nanostructures. (a) Small particle sizes and (b) large particle sizes.

distinguished at 390, 440, and 470 nm. The maximum photoluminescence intensity corresponds to the WZO-2S sample, while the minimum intensity is demonstrated by the WZO-5S sample.

An opposite situation was observed in the photoluminescence (PL) spectra for the WZO-1L, 2L, 3L, 4L, and 5L

samples (Figure 8b). The intense emission is recorded upon excitation at a wavelength of 305 nm in the 350–900 nm spectral region. For samples WZO-1L and WZO-2L, the emission is similar to that described above and 3 emission bands can be distinguished at 390, 440, and 470 nm. For samples WZO-4L and WZO-5L, an intense nonelementary band is observed in the region of 450–900 nm. Sample WZO-3L exhibits intense emission consisting of a number of overlapping bands in the range 390–900 nm. Additional emission bands can be identified at 440, 460, 500, 530, 580, and 620 nm in PL spectra. The green emission at 530 nm is attributed to the radiative recombination of simple ionized oxygen vacancies. This is very often observed in the oxygen-deficient ZnO material.¹⁴ The bands centered at 390 and 440 nm, respectively, are attributed to interband transitions and emission from deep levels in the bandgap region.^{37–40} The bands at 460 and 500 nm are possibly related to emissions of V_O-Zn_i complexes (Zinc interstitials (Zn_i) with oxygen vacancies (V_O)).³⁸ Small differences in the energies of these complexes may be due to their different distances in the ZnO caristall lattice.^{41,42} The emission band at 620 nm is attributed to radiative interband recombination of electrons and holes in WS₂.^{43,44}

3.4. Photoelectrochemical Measurements. Photoelectrochemical (PEC) investigations were conducted on a potentiostat-galvanostat P-40X in order to evaluate the potential of the prepared WZO nanostructures as materials for photoelectrodes in photoelectrochemical cells. The PEC measurements were performed in a three-electrode cell in which WZO-coated graphite, graphite, and Ag/AgCl electrodes were employed as working, counter, and reference electrodes, respectively. This protocol was chosen since it is cost-effective and quite efficient. A 0.1 M solution of NaOH was used as the electrolyte in the cell. The maximum potential applied to the working electrode was 2 V in cyclic voltammetry experiments. The potential scanning rate was 5 mV/s. The working electrode was prepared by embedding WZO nanostructures into conductive polymer glue matrices, and highly conductive graphite electrodes were coated with WZO-based compositions. Figure 9a demonstrates the cyclic voltammograms and Nyquist plots on the photoelectrochemical cell with a WSO-3L nanodecorated photoanode. The measurements were conducted under natural (dark) conditions and under the irradiation of a Xe 150W lamp (light) in order to evaluate the contribution of the WZO-decorated working electrode to the photocurrent induced in the photoelectrochemical cell. For the light conditions, the photoelectrochemical measurements were accompanied by increased intensive gaseous H₂ and O₂ gas evolution at the counter and working electrodes, respectively.

The electrochemical impedance curve recorded for the WZO-3L nanostructures is shown in Figure 9b. For this WZO-3L-decorated graphite electrode, the impedance measurements for both the dark and light conditions were conducted at 50 different frequencies. In all scanning regions (between 12.5 and 20.5 Ω of the real impedance), the imaginary impedance is lower for the light experience, whereas the difference between light and dark conditions tends to be 1.8 Ω on the Nyquist plot. Therefore, the WZO-3L-based electrode shows better conductivity under light conditions than in the dark during photoelectrochemical measurements.

Table 3 summarizes the parameters of the photoelectrochemical measurements for all WZO nanoheterostructures

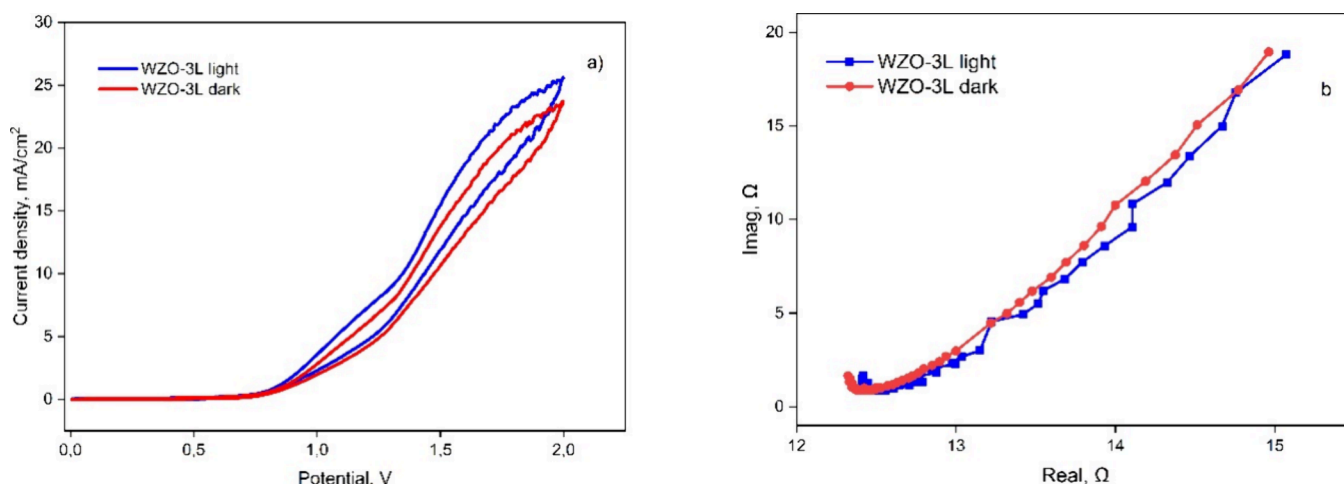


Figure 9. Cyclic voltammograms (a) and Nyquist plots (b) of WS_2 -ZnO nanostructures under light (blue) and dark (red) conditions.

Table 3. Current Densities Obtained from C–V Curves of WZO-Decorated Photoelectrodes^a

sample name	current (mA/cm ²)		ΔJ (mA/cm ²)
	light	dark	
WZO-1L	2.628	1.875	0.753
WZO-1S	6.750	4.186	2.564
WZO-2L	10.019	9.390	0.627
WZO-2S	10.657	10.083	0.573
WZO-3L	25.671	23.702	1.969
WZO-3S	6.667	6.049	0.618
WZO-4L	15.725	14.892	0.833
WZO-4S	7.925	7.262	0.663
WZO-5L	10.591	9.642	0.949
WZO-5S	3.851	2.715	1.136

^a ΔJ the difference in current under light on–off states.

under the light and dark conditions. The highest difference ΔJ in current under light on–off states was found for the WZO-1S-decorated photoelectrodes.

The results of cyclic voltammetry were compared to literature data. The current density is about zero mA/cm² at the potentials up to 0.7 V. The further increase of potential results in the sharp growth of the current density that is much higher than it is known in the literature.⁴⁵

Comparison of Nyquist plots of our WS_2 -ZnO heterostructures and WS_2 -ZnO nanocomposite^{36,45} revealed the lower values of our samples' impedance. Therefore, the charge transfer resistance is significantly low. Thus, it makes the movement of the charge carriers on the interface easy and faster and enhances photocatalytic efficiency.

4. CONCLUSIONS

The present paper describes the successful synthesis of WS_2 -ZnO nanostructures by using electrospray erosion of zinc granules in an aqueous solution of hydrogen peroxide. To evaluate the role of hydrogen peroxide as a liquid medium oxidizer, four different volume concentrations of hydrogen peroxide aqueous solutions were used in the ESE synthesis. TEM observations demonstrated that the ESE products represent binary heterostructures between the WS_2 nanoparticles (40–80 nm in diameter) and ZnO nanoparticles (10–20 nm in diameter). Intense emission is recorded upon excitation at a wavelength of 305 nm in the 350–900 nm

spectral region. For samples WZO-1L and WZO-2L, the emission is similar, and 3 emission bands can be distinguished at 390, 440, and 470 nm. Cyclic voltammetry measurements showed a photocurrent of about 2.564 mA/cm² in a classical three-electrode cell with a WZO-decorated working electrode in 0.1 M NaOH electrolyte, with vigorous hydrogen evolution. The obtained materials possess good potential for use as a photoanode material for photoelectrochemical water splitting to generate hydrogen for green energy applications.

AUTHOR INFORMATION

Corresponding Author

Johannes Potgieter – Department of Natural Sciences, Manchester Metropolitan University, Manchester M15 6GD, U.K.; School of Chemical and Metallurgical Engineering, University of the Witwatersrand, Wits 2050, South Africa; orcid.org/0000-0003-2833-7986; Email: h.potgieter@mmu.ac.uk

Authors

Kakhramon Rakhimbekov – Kizhner Research Center, School of Advanced Manufacturing Technologies, Tomsk Polytechnic University, Tomsk 634050, Russia

Damir Valiev – Division for Materials Science, School of Advanced Manufacturing Technologies, Tomsk Polytechnic University, Tomsk 634050, Russia

Vladimir An – Kizhner Research Center, School of Advanced Manufacturing Technologies, Tomsk Polytechnic University, Tomsk 634050, Russia

Anna Blinova – Kizhner Research Center, School of Advanced Manufacturing Technologies, Tomsk Polytechnic University, Tomsk 634050, Russia; orcid.org/0009-0005-8297-6430

Natalia Usoltseva – Kizhner Research Center, School of Advanced Manufacturing Technologies, Tomsk Polytechnic University, Tomsk 634050, Russia; orcid.org/0000-0002-3174-0242

Alexey Pustovalov – Research and Manufacturing Laboratory “Pure Water”, School of Advanced Manufacturing Technologies, Tomsk Polytechnic University, Tomsk 634050, Russia

Maksim Vasilevichev – Kizhner Research Center, School of Advanced Manufacturing Technologies, Tomsk Polytechnic University, Tomsk 634050, Russia

Alexandra Platonova – Kizhner Research Center, School of Advanced Manufacturing Technologies, Tomsk Polytechnic University, Tomsk 634050, Russia

Sergey Stepanov – Division for Materials Science, School of Advanced Manufacturing Technologies, Tomsk Polytechnic University, Tomsk 634050, Russia

Dmitri Kokotov – Division for Materials Science, School of Advanced Manufacturing Technologies, Tomsk Polytechnic University, Tomsk 634050, Russia

Vladimir Sypchenko – Division for Experimental Physics, School of Nuclear Science & Engineering, Tomsk Polytechnic University, Tomsk 634050, Russia

Complete contact information is available at:

<https://pubs.acs.org/10.1021/acsaem.4c01488>

Author Contributions

Conceptualization, V.A., J.H.P., K.R., and D.V.; methodology, V.A., K.R., A.P., D.V., and N.U.; validation, V.A., K.R., and D.V.; formal analysis, V.A., K.R., and N.U.; investigation, V.A., K.R., A.P., A.B., D.V., and D.K.; data curation, K.R., V.A., A.B., and M.V.; writing – original draft preparation, K.R., J.H.P., and V.A.; writing – review and editing, K.R., J.H.P., V.A., D.V., N.U.; visualization, V.A., K.R., and D.V.; supervision, V.A. All authors have read and agreed to the published version of the manuscript.

Notes

The authors declare no competing financial interest.

ACKNOWLEDGMENTS

This research was supported by TPU development program Priority 2030 (Priority-2030-NIP/EB- 113-375-2023). The research was carried out using the equipment of the Centre for Sharing Use «Nanomaterials and Nanotechnologies» of Tomsk Polytechnic University supported by the RF Ministry of Education and Science project #075–15–2021–710.

REFERENCES

- (1) Wu, Y.; Yue, Z.; Liu, A.; Yang, P.; Zhu, M. P-Type Cu-Doped $Zn_{0.3}Cd_{0.7}S$ /Graphene Photocathode for Efficient Water Splitting in a Photoelectrochemical Tandem Cell. *ACS Sustain Chem. Eng.* **2016**, *4* (5), 2569–2577.
- (2) Liu, X.; Shan, C.; Jiao, C.; Wang, S.; Zhao, H.; Shen, D. Pure ultraviolet emission from ZnO nanowire-based *p-n* heterostructures. *Opt. Lett.* **2014**, *39* (3), 422–425.
- (3) Gogurla, N.; Sinha, A. K.; Santra, S.; Manna, S.; Ray, S. K. Multifunctional Au-ZnO plasmonic nanostructures for enhanced UV photodetector and room temperature NO sensing devices. *Sci. Rep.* **2014**, *4*, No. 6483.
- (4) Jalal, R.; Goharshadi, E.; Abareshi, M.; Moosavi, M.; Yousefi, A.; Nancarrow, P. ZnO nanofluids: Green synthesis, characterization, and antibacterial activity. *Mater. Chem. Phys.* **2010**, *121* (1–2), 198–201.
- (5) Singh, A.; Kumar, P. Structural, morphological and optical properties of sol gel processed CdZnO nanostructured films: effect of precursor solvents. *Int. Nano Lett.* **2013**, *3*, 57.
- (6) Stanković, A.; Dimitrijević, S.; Uskoković, D. Influence of size scale and morphology on antibacterial properties of ZnO powders hydrothermally synthesized using different surface stabilizing agents. *Colloids Surf., B* **2013**, *102*, 21–28.
- (7) Talebian, N.; Amininezhad, S.; Doudi, M. Controllable synthesis of ZnO nanoparticles and their morphology-dependent antibacterial and optical properties. *J. Photochem. Photobiol. B, Biol.* **2013**, *120*, 66–73.
- (8) Hafez, E. E.; Hassan, H. S.; Elkady, M. F.; Salama, E. Assessment of antibacterial activity for synthesized zinc oxide nanorods against plant pathogenic strains. *Int. J. Sci. Technol. Res.* **2014**, *3* (9), 318–324.
- (9) Kołodziejczak-Radzimska, A.; Jesionowski, T. Zinc Oxide-From Synthesis to Application: A Review. *Materials* **2014**, *7* (4), 2833–2881.
- (10) Major, S.; Banerjee, A.; Chopra, K. L. Optical and electronic properties of zinc oxide films prepared by spray pyrolysis. *Thin Sol. Films* **1985**, *125* (1–2), 179–185.
- (11) Hu, J.; Gordon, R. G. Textured Fluorine Textured fluorine-doped ZnO films by atmospheric pressure chemical vapor deposition and their use in amorphous silicon solar cells. *Sol. Cells* **1991**, *30* (1–4), 437–450.
- (12) Gong, Y.; Zou, C.; Yao, Y.; Fu, W.; Wang, M.; Yin, G.; Huang, Zh.; Liao, X.; Chen, X. A facile approach to synthesize rose-like ZnO/reduced graphene oxide composite: Fluorescence and photocatalytic properties. *J. Mater. Sci.* **2014**, *49* (16), 5658–5666.
- (13) Zhu, Y.; Deng, F.; Feng, L.; Ding, H.; Ismat Shah, S.; Ni, C. Hierarchical rhombus-shaped ZnO array: synthesis, formation mechanism and solar cell application. *J. Alloys & Comp.* **2014**, *607*, 132–138.
- (14) Rauwel, E.; Galeckas, A.; Rauwel, P.; Sunding, M. F.; Fjellva, H. Precursor-Dependent Blue-Green Photoluminescence Emission of ZnO Nanoparticles. *J. Phys. Chem. C* **2011**, *115* (51), 25227–25233.
- (15) Kumar, S.; Rao, K. Zinc oxide based photocatalysis: tailoring surface-bulk structure and related interfacial charge carrier dynamics for better environmental applications. *RSC Adv.* **2015**, *5*, 3306–3351.
- (16) Barka-Bouaifel, F.; Sieber, B.; Bezzi, N.; Benner, J.; Roissel, P.; Boussekey, L.; Szunerits, S.; Boukherroub, R. Synthesis and Photocatalytic Activity of Iodine-Doped ZnO Nanoflowers. *J. Mater. Chem.* **2011**, *21* (29), 10982–10989.
- (17) Djurišić, A. B.; Chen, X.; Leung, Y. H.; Ng, A. M. C. ZnO nanostructures: growth, properties and applications. *J. Mater. Chem.* **2012**, *22* (14), 6526–6535.
- (18) Nasr, M.; Benhamou, L.; Kotbi, A.; Rajput, N. S.; Campos, A.; Lahmar, A.-I.; Hoummada, K.; Kaja, K.; El Marssi, M.; Jouiad, M. Photoelectrochemical Enhancement of Graphene@WS₂ Nanosheets for Water Splitting Reaction. *Nanomaterials* **2022**, *12* (11), 1914.
- (19) Ding, Q.; Song, B.; Xu, P.; Jin, S. Efficient Electrocatalytic and Photoelectrochemical Hydrogen Generation Using MoS₂ and Related Compounds. *Chem.* **2016**, *1*, 699–726.
- (20) Shiraz, H.; Crispin, X.; Berggren, M. Transition metal sulfides for electrochemical hydrogen evolution. *Int. J. Hydr. Ener.* **2021**, *46* (47), 24060–24077.
- (21) Chu, D.; Li, K.; Liu, A.; Huang, J.; Zhang, C.; Yang, P.; Du, Y.; Lu, C. Zn-doped hematite modified by graphene-like WS₂: A p-type semiconductor hybrid photocathode for water splitting to produce hydrogen. *Int. J. Hydrogen Energy* **2018**, *43* (15), 7307–7316.
- (22) Lin, Y. P.; Polyakov, B.; Butanovs, E.; Popov, A. A.; Sokolov, M.; Bocharov, D.; Piskunov, S. Excited States Calculations of MoS₂@ZnO and WS₂@ZnO Two-Dimensional Nanocomposites for Water-Splitting Applications. *Energies* **2022**, *15* (1), 150.
- (23) Wang, S.; Tian, H.; Ren, C.; Yu, J.; Sun, M. Electronic and optical properties of heterostructures based on transition metal dichalcogenides and graphene-like zinc oxide. *Sci. Reports* **2018**, *8*, 12009.
- (24) Guan, Y.; Yao, H.; Zhan, H.; Wang, H.; Zhou, Y.; Kang, J. Optoelectronic properties and strain regulation of the 2D WS₂/ZnO van der Waals heterostructure. *RSC Adv.* **2021**, *11*, 14085–14092.
- (25) An, V.; Liu, B. Synthesis of multilevel ZnS/ZnO nanostructures by electrospray erosion. *Chalcogenide Lett.* **2015**, *12* (12), 639–644.
- (26) Aleksandrova, M.; Ivanova, T.; Hamelmann, F.; Strijkova, V.; Gesheva, K. Study of Sputtered ZnO:Ga₂O₃ Films for Energy Harvesting Applications. *Coatings* **2020**, *10* (7), 650.
- (27) Vaziri, H. S.; Shokuhfar, A.; Afghahi, S. S. S. Synthesis of WS₂/CNT hybrid nanoparticles for fabrication of hybrid aluminum matrix nanocomposite. *Mater. Res. Express* **2020**, *7* (2), No. 025034.
- (28) Kılınç, N.; Arda, L.; Öztürk, S.; Öztürk, Z. Z. Structure and electrical properties of Mg-doped ZnO nanoparticles. *Cryst. Res. Technol.* **2010**, *45* (5), 529–538.

- (29) Kwon, Y. J.; Kim, K. H.; Lim, C. S.; Shim, K. B. Characterization of ZnO nanopowders synthesized by the polymerized complex method via an organochemical route. *J. Ceram. Process. Res.* **2002**, *3*, 146–149.
- (30) Zare, M.; Namratha; Byrappa, K.; Surendra, D. M.; Yallappa, S.; Hungund, B. Surfactant assisted solvothermal synthesis of ZnO nanoparticles and study of their antimicrobial and antioxidant properties. *J. Mater. Sci. & Technol.* **2018**, *34* (6), 1035–1043.
- (31) Berkdemir, A.; Gutiérrez, H. R.; Botello-Méndez, A. R.; Perea-López, N.; Elías, A. L.; Chia, C. I.; Wang, B.; Crespi, V. H.; López-Urías, F.; Charlier, J. C.; Terrones, H.; Terrones, M. Identification of individual and few layers of WS₂ using Raman Spectroscopy. *Sci. Rep.* **2013**, *3* (1), No. 1755.
- (32) Song, Y.; Zhang, S.; Zhang, C.; Yang, Y.; Lv, K. Raman Spectra and Microstructure of Zinc Oxide irradiated with Swift Heavy Ion. *Crystals.* **2019**, *9* (8), 395.
- (33) Silambarasan, M.; Saravanan, S.; Soga, T. Mn-Doped ZnO Nanoparticles Prepared by Solution Combustion Method. *e-J. Surf. Sci. Nanotechnol* **2014**, *12*, 283–288.
- (34) Calizo, I.; Alim, K. A.; Fonoberov, V. A.; Krishnakumar, S.; Shamsa, M.; Balandin, A. A.; Kurtz, R. Micro-Raman spectroscopic characterization ZnO quantum dots, nanocrystals, and nanowires. In *Quantum Dots, Particles, and Nanoclusters IV*; SPIE: 2007, 6481, 96-103. DOI: .
- (35) Li, X.; Wang, X.; Luo, J.; Jiang, J.; Ding, K.; Ye, L.; Xiong, Yu.; Pang, D.; Li, H.; Yu, P.; Kong, Ch.; Ye, L.; Zhang, H.; Li, W. Fully-transparent self-powered ultraviolet photodetector based on GaO_x/ZnO heterojunction for solar-blind imaging. *Materials Today Communications* **2023**, *35*, No. 106118.
- (36) Tyagi, N.; Singh, M. K.; Khanuja, M. WS₂ nanosheets modified via ZnO nanorods (2D/1D) nanocomposite: An efficient photocatalyst for the removal of Cr (VI), humic acid and textile dyes from wastewater. *Ceram. Int.* **2023**, *49* (22), 34447–34460.
- (37) Cetin, S. S.; Uslu, I.; Aytimur, A.; Ozcelik, S. Characterization of Mg doped ZnO nanocrystallites prepared via electrospinning. *Ceram. Int.* **2012**, *38* (5), 4201–4208.
- (38) Kondal, N.; Tiwari, S. Selectively enhanced oxygen vacancies in undoped polycrystalline ZnO as a consequence of Multi-Step Sintering. *Ceram. Int.* **2017**, *43* (13), 10347–10352.
- (39) Yu, Y.; Kim, G.; Min, B.; Kim, S. Optical characteristics of Ge doped ZnO compound. *J. Eur. Ceram. Soc.* **2004**, *24* (6), 1865–1868.
- (40) Panatarani, C.; Muharam, D.; Wibawa, B.; Joni, I. Blue Luminescent of ZnO:Zn Nanocrystal Prepared by One Step Spray Pyrolysis Method. *Mater. Sci. Forum* **2013**, *737*, 20–27.
- (41) Lin, K. F.; Cheng, H. M.; Hsu, H. C.; Hsieh, W. F. Band gap engineering and spatial confinement of optical phonon in ZnO quantum dots. *Appl. Phys. Lett.* **2006**, *88* (26), No. 263117.
- (42) Das, J.; Mishra, D.; Srinivasu, V.; Sahu, D.; Roul, B. Photoluminescence and Raman studies for the confirmation of oxygen vacancies to induce ferromagnetism in Fe doped Mn:ZnO compound. *J. Magn. & Magn. Mater.* **2015**, *382*, 111–116.
- (43) Okada, M.; Sawazaki, T.; Watanabe, K.; Taniguchi, T.; Hibino, H.; Shinohara, H.; Kitaura, R. Direct chemical vapor deposition growth of WS₂ atomic layers on hexagonal boron nitride. *ACS Nano* **2014**, *26* (8), 8273.
- (44) Zeng, H.; Liu, G.-B.; Dai, J.; Yan, Y.; Zhu, B.; He, R.; Xie, L.; Xu, S.; Chen, X.; Yao, W.; Cui, X. Optical signature of symmetry variations and spin-valley coupling in atomically thin tungsten dichalcogenides. *Sci. Rep.* **2013**, *3*, 1608.
- (45) Pataniya, P. M.; Late, D.; Sumesh, C. K. Photosensitive WS₂/ZnO Nano-Heterostructure-Based Electrocatalysts for Hydrogen Evolution Reaction. *ACS Appl. Energy Mater.* **2021**, *4*, 755–762.